Analysis of two partially-saturated-cell methods for lattice Boltzmann simulation of granular suspension rheology

Analysis of two partially-saturated-cell methods for lattice Boltzmann simulation of granular suspension rheology

Tim Najuch*, Jin Sun*

School of Engineering, The University of Edinburgh, Thomas Bayes Road, EH9 3FG Edinburgh, United Kingdom

Abstract

The lattice Boltzmann method (LBM) has been widely used to simulate fluid–solid flows with various approaches to couple the two phases. We study the partially-saturated-cell (PSC) approach proposed by Nobel and Torczynski [A lattice-Boltzmann method for partially saturated computational cells. International Journal of Modern Physics, 9(8):1189–1201, 1998], which modifies the LB equation by an additional solid collision term weighted by the lattice solid fraction. We analyse two different PSC schemes with regard to its capability of accurately computing the hydrodynamic stresslet, which is essential to computing the stress, hence the rheology of suspensions of granular particles. Through simulations of single and pair particles in a simple shear flow field, we show that a commonly used solid collision term based on non-equilibrium bounce-back fails to correctly capture the stresslet, although can result in a numerically accurate hydrodynamic torque, when compared to the analytical solutions. In contrast, a model using superposition, which has neither hitherto been analysed nor extensively applied, is demonstrated to be able to accurately calculate both the stresslet and

*Corresponding authors: Tim.Najuch@ed-alumni.net / J.Sun@ed.ac.uk

the torque. We finally highlight the importance of using the correct model when simulating suspension rheology, showing the viscosity obtained in simulations of hundreds of mono-disperse particles at various solid fractions sheared homogeneously using the Lees-Edwards boundary condition.
Keywords: Lattice Boltzmann method, LBM-DEM, Partially saturated cell method, Suspensions, Fluid-solid coupling, Stresslet

1. Introduction

Flows of granular suspensions are ubiquitous in nature and industry, e.g. debris flows, paste extrusion, or fluidised beds. Simulation is a powerful tool to study the underlying physical mechanisms in these processes. The lattice Boltzmann method, among various methodologies developed, has gained popularity due to its simplicity in implementation and efficiency in parallelisation. The applicability and accuracy, however, depend on the fluid–solid coupling approach employed. One of the earliest and most used was developed by Ladd (1994a,b) and based on a straightforward bounce back boundary condition on the particle surface. Improvements with regard to the momentum exchange were suggested (Aidun and Lu, 1995; Aidun et al., 1998). An immersed boundary method was also developed by Feng and Michaelides (2005).

An alternative approach, extending the LB equation with a collision term taking into account the effects of the solid phase inside particles, was proposed by Noble and Torcyznski (1998). Two different models for the solid phase collision term were given, viz., the non-equilibrium bounce back (BB) and the superposition (SP) model. The fluid and solid collision terms are appropriately weighted by a weighting function of solid fraction, the proportion of a lattice cell occupied by a particle. This method is termed

the partially saturated cell (PSC) method. Comparing to other coupling methods, it allows for large numbers of nonconforming, evolving boundaries but retaining the advantages of the conventional LBM, i.e., a collision step is local to nodes, and is thus well suited for simulating suspensions with moving particles. To successfully apply the PSC method to suspension rheology, however, it is necessary to determine the validity and accuracy of the method against rheological measures.

Previous validation studies have mostly focused on analysis of hydrodynamic force and torque on particles. For example, Owen et al. (2011) simulated flow around circular and rectangular objects at Reynolds number, $0.5 \leq Re \leq 40$, and Couette flow in two dimension (2D); as well as flow through a periodic array of spheres and around a single sphere, and multiple particles sedimentation in 3D with the BB model. The results were shown to largely agree with the known experimental and simulation results in the literature. It is interesting to note the different accuracy levels found for the BB and SP models: the BB model captures the torque in the Couette flow more accurately; while the SP models produces smaller errors in the maximum velocity at the rotating cylinder surface (Owen et al., 2011). A different implementation of the PSC models in coupled Palabos (LBM) and LIGGGHTS (discrete element method) solvers (Seil, 2016) has also been shown to produce correct drag, lift, and torque values for flow around spheres in 2D or 3D.

In few studies of rheology, Zhou et al. (2011) obtained the viscosity of dilute suspensions with solid fractions ϕ ranging $0 < \phi < 0.25$ using a modified PSC method and Lorenz et al. (2018) produced the viscosity for $0.25 < \phi < 0.56$ employing the BB model in simple shear flow. Both obtained the correct trend of viscosity increasing with the increasing solid

fraction.

However, none of the previous work has analysed the accuracy of either the BB or the SP models in the computation of hydrodynamic stresslet, the symmetric part of the first moment of the hydrodynamic force on particles. As stresslet is an essential component of the total stress in a suspension, accurately computing the stresslet is thus fundamental to studying rheology of suspensions. In this paper, we focus on analysing the accuracy of the two PSC methods in capturing stresslet through comparing the results for single and pair interacting particles in a linear shearing flow field to analytical solutions. The mechanism leading to the discrepancies between the BB and SP models is studied by looking into the fluid slip velocity and hydrodynamic forces over a particle volume.

Furthermore, the effect of the two collision models on the macroscopic fluid mass and momentum conservation equations is examined using the Chapman-Enskog analysis, which has hitherto not been performed for the PSC method. This further elucidates the difference between the two models. We note from the outset that the original PSC method as proposed by Noble and Torcyznski (1998) has been employed for this study. The modified schemes (Holdych, 2003; Zhou et al., 2011) were not used due to numerical instability issues as reported by other researchers (Cook et al., 2004; Wang et al., 2016) and encountered in our other studies (refer to Appendix A for an analysis of the Holdych scheme.).

The rest of the paper is organised as follows. The lattice Boltzmann method and the PSC coupling method are described in Section 2. In Section 3, we first theoretically analyse the PSC method, then present simulation results of single and two particles sheared between two parallel walls and finally demonstrate the importance of accurate computation of stresslet

by comparison of simulated suspension viscosities at different solid fractions under simple shear to known analytical and experimental results. The results are summarised in Section 4 with recommendation of applying the SP model for suspension rheology simulation.

2. Methodology

A methodology of simulating dynamics of fluid–particle systems is described in this section. The fluid dynamics is resolved by the lattice Boltzmann method (LBM), while the particle dynamics by the discrete element method (DEM). The coupling is achieved through introducing an additional collision term in LBM. These components will be described in the following. The implementation of method in numerical code follows the work by Seil (2016) and will not be detailed here.

2.1. Lattice Boltzmann method

The lattice Boltzmann method (LBM) evaluates the discretised Boltzmann equation of the fluid particle distribution function $f(\mathbf{x}, \mathbf{u}, t)$ on a lattice. On each lattice node, a discrete particle distribution function $f_i(\mathbf{x}, t)$ is subject to a collision and a streaming step. During the collision step, $f_i(\mathbf{x}, t)$ is relaxed towards an equilibrium distribution function $f_i^{eq}(\mathbf{x}, \mathbf{u}, t)$, where $\mathbf{u}$ is the macroscopic fluid velocity. In the simplest case, the Bhatnagar-Gross-Krook (BGK) collision term (Bhatnagar et al., 1954), is described by a single relaxation parameter τ, i.e.

$$\Omega_i^{BGK} = \frac{\Delta t}{\tau}(f_i^{eq}(\mathbf{x}, \mathbf{u}, t) - f_i(\mathbf{x}, t)) \; . \tag{1}$$

After the collision step, each distribution is moved according to pre-defined lattice velocities $\mathbf{c}_i$ to adjacent lattice nodes during the streaming step.

Streaming and BGK collision step can be summarised to the discrete lattice Boltzmann equation:

$$f_i(\mathbf{x} + \mathbf{c}_i\Delta t, t + \Delta t) = f_i(\mathbf{x}, t) + \Omega_i^{BGK}\,, \tag{2}$$

where the lattice velocities $\mathbf{c}_i$ are appropriately chosen to recover the equations for mass and momentum conservation (Navier-Stokes equations) and the relaxation parameter τ can be related to the fluid viscosity $\nu = (\tau - 0.5)/3$ (Succi, 2001; Chen and Doolen, 1998). Macroscopic fluid density and velocity can be obtained by computing the zeroth and first moments of the particle distribution function, i.e. $\rho = \sum_i f_i(\mathbf{x}, t)$ and $\rho\mathbf{u} = \sum_i f_i(\mathbf{x}, t)\mathbf{c}_i$.

2.2. Fluid-solid coupling

2.2.1. The partially saturated cell method

Noble and Torcyznski (1998) proposed that the presence of particles can be accounted for by including an additional collision term Ω^s and a weighting function $B(\mathbf{x}, \tau)$ for the solid fraction of the lattice node at $\mathbf{x}$, so that Eq. (2) reads:

$$f_i(\mathbf{x} + \mathbf{c}_i\Delta t, t + \Delta t) = f_i(\mathbf{x}, t) + (1 - B(\mathbf{x}, \tau))\Omega_i^{BGK} + B(\mathbf{x}, \tau)\Omega_i^s\,. \tag{3}$$

Two different collision terms for the solid phase Ω^s were suggested by Noble and Torcyznski (1998). The first model, which is widely used in the literature, reads:

$$\Omega_i^s = f_{-i}(\mathbf{x}, t) - f_i(\mathbf{x}, t) + f_i^{eq}(\rho, \mathbf{u}_s) - f_{-i}^{eq}(\rho, \mathbf{u})\,, \tag{4}$$

where velocity of fluid $\mathbf{u}$ and particle $\mathbf{u}_s$ are individually considered on each lattice node. f_{-i} stands for the distribution functions with velocity in the opposite direction of f_i. Noble and Torcyznski (1998) described Eq. (4)

as being inspired by the non-equilibrium bounce back boundary condition, hence the abbreviation BB method used in this work.

The second model reads

$$\Omega_i^s = f_i^{eq}(\rho, \mathbf{u}_s) - f_i(\mathbf{x}, t) + \left(1 - \frac{\Delta t}{\tau}\right) \left[f_i(\mathbf{x}, t) - f_i^{eq}(\rho, \mathbf{u})\right] , \tag{5}$$

described as the superposition method by Noble and Torcyznski (1998) and hence abbreviated as the SP method.

The weighting function can assume a linear relationship to the lattice node solid fraction according to (Noble and Torcyznski, 1998)

$$B(\mathbf{x}, \tau) = \varepsilon_s , \tag{6}$$

or a non-linear form

$$B(\mathbf{x}, \tau) = \frac{\varepsilon_s(\tau/\Delta t - 0.5)}{(1 - \varepsilon_s) + (\tau/\Delta t - 0.5)} , \tag{7}$$

but other options could be conceived as for example by Zhou et al. (2011). The solid fraction computation is based on a "brute force" approach as

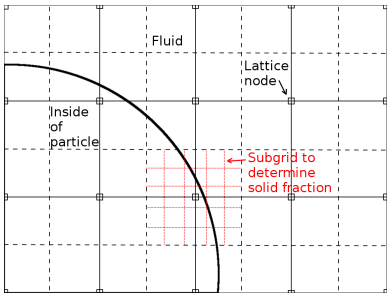

Figure 1: Schematic of the solid fraction computation for nodes covered by particles.

depicted in Fig. 1. For each lattice node, the lattice node itself acts as the centre of a surrounding cubic element of the size of a lattice cell. The cubic volume is equally divided into smaller cubes with N_{SGR} number of

cubes in each coordinate direction, i.e. N_{SGR}^3 smaller cubes in total for a three dimensional system. The number of cubes within the particle volume related to the total number of cubes provides the lattice node solid fraction. An increase in this subgrid resolution (SGR) leads to a more accurate solid fraction computation, but also an increased computational overhead.

The local hydrodynamic force exerted by the fluid on a solid node can be calculated from the local momentum transfer between the fluid and the solid domains

$$\mathbf{F}^{\mathrm{H}}(\mathbf{x}) = \frac{h^d}{\Delta t} B(\mathbf{x}) \sum_i \Omega_i^s \mathbf{c}_i \,, \tag{8}$$

and hence the torque

$$\mathbf{T}^{\mathrm{H}}(\mathbf{x}) = (\mathbf{x} - \mathbf{x}_s) \times \mathbf{F}^{\mathrm{H}}(\mathbf{x}) \,, \tag{9}$$

where $\mathbf{x}_s$ is the particle centre position, h the lattice spacing and d the dimension. The total hydrodynamic force and torque acting on a particle can be obtained by summing the nodal values over all solid covered lattice nodes.

2.2.2. Stresslet

Batchelor (1970) derived the formula for bulk stress of a suspension, which has been used in previous LBM simulations by, e.g., Haddadi and Morris (2014) or Daghoogi and Borazjani (2015),

$$\Sigma_{ij} = \frac{1}{V} \int_V (\sigma_{ij} - \rho u_i' u_j') dV \,, \tag{10}$$

where V is the suspension volume of interest. For a Newtonian fluid,

$$\Sigma_{ij} = \frac{1}{V} \int_{V - \sum V_p} \left[-p\delta_{ij} + \mu \left(\frac{\partial u_i}{\partial x_j} + \frac{\partial u_j}{\partial xi} \right) \right] dV + \frac{1}{V} \sum \int_{V_p} \sigma_{ij} dV - \frac{1}{V} \int_V \rho u_i' u_j' dV \,, \tag{11}$$

where V_p is the particle volume. The particle stress can be simplified by application of the divergence theorem (Batchelor, 1970; Haddadi and Morris, 2014) and leads to three stress contributions, viz. stresslet, acceleration stress and Reynolds stress. For low Reynolds numbers and without external couples imposed on the suspended particles, the particle stress, i.e. the last two terms in Eq. (11), reduces to the total stresslet divided by the averaging volume:

$$\Sigma_{ij}^{P} = \frac{1}{V}\sum_{\alpha=1}^{N} S_{ij}^{\alpha} = \frac{1}{V}\sum_{\alpha=1}^{N}\frac{1}{2}\int_{A^{\alpha}}(\sigma_{ik}x_j + \sigma_{jk}x_i)n_k dA \;, \tag{12}$$

where A^{α} denotes the surface of particle α. The stresslet arising from fluid action on each particle can be computed in LBM simulations by relating the surface traction to the hydrodynamic forces $\mathbf{F}^{\mathrm{H}}$ (cf. Eq. (8)) acting on each node covered by the particle, i.e., $\sigma_{ik}n_k dA = F_i^{\mathrm{H}\beta}$

$$S_{ij}^{\alpha} = \frac{1}{2}\sum_{\beta=1}^{N_{\mathrm{nodes}}}\left(F_i^{\mathrm{H}\beta}x_j + F_j^{\mathrm{H}\beta}x_i\right) \;, \tag{13}$$

where the vector $\mathbf{x}$ points from the particle centre to the lattice node on which $\mathbf{F}^{\mathrm{H}}$ acts and $dA = h^2$ is taken to be the area covered by one lattice.

2.3. Discrete element method

Each particle is tracked with by solving Newton's second law for translational and angular motion with the discrete element method (Cundall and Strack, 1979). The particle motion equation can include the forces/torques due to mechanical particle–particle interactions $\mathbf{F}^{\mathrm{C}}/\mathbf{T}^{\mathrm{C}}$ and hydrodynamic interactions $\mathbf{F}^{\mathrm{H}}/\mathbf{T}^{\mathrm{H}}$ determined by the LBM, as

$$m_i\frac{\mathrm{d}\mathbf{x}_i^2}{\mathrm{d}^2 t} = \mathbf{F}_i^{\mathrm{C}} + \mathbf{F}_i^{\mathrm{H}} \;, \tag{14}$$

for translation motion and similarly for the angular motion

$$\mathbf{J}_i \frac{\mathrm{d}\boldsymbol{\omega}_i}{\mathrm{d}t} = \mathbf{T}_i^{\mathrm{C}} + \mathbf{T}_i^{\mathrm{H}} \ , \tag{15}$$

where mass, position, moment of inertia and angular velocity of particle i are denoted by m_i, $\mathbf{x}_i$, $\mathbf{J}_i$ and $\boldsymbol{\omega}_i$, respectively.

3. Results

3.1. Theoretical analysis of the LBM-DEM coupling

We first rewrite the modified LB Eq. (3) into a form of the single phase LB equation Eq. (2) with an additional term F_i,

$$f_i(\mathbf{x} + \mathbf{c}_i\Delta t, t + \Delta t) = f_i(\mathbf{x}, t) + \Omega_{BGK}(\mathbf{x}, \mathbf{u}, t) + F_i(\mathbf{x}, \mathbf{u}, t) \ . \tag{16}$$

For the BB and SP methods, F_i reads

$$F_i^{BB}(\mathbf{x}, t) = B(\mathbf{x}, \tau)\Bigg(\frac{\Delta t}{\tau}\left[f_i(\mathbf{x}, t) - f_i^{eq}(\mathbf{x}, \mathbf{u}, t)\right] + f_{-i}(\mathbf{x}, t) - f_i(\mathbf{x}, t) + f_i^{eq}(\mathbf{x}, \mathbf{u}_s, t) - f_{-i}^{eq}(\mathbf{x}, \mathbf{u}, t)\Bigg) \ , \tag{17}$$

and

$$F_i^{SP}(\mathbf{x}, t) = B(\mathbf{x}, \tau)\left(f_i^{eq}(\mathbf{x}, \mathbf{u}_s, t) - f_i^{eq}(\mathbf{x}, \mathbf{u}, t)\right) \ , \tag{18}$$

respectively. This additional term leads to an external force at the macroscopic level,

$$\mathbf{F} = \frac{h^d}{\Delta t}\sum_n B_n \rho(\mathbf{u}_s - \mathbf{u}) \ , \tag{19}$$

as shown by taking the first moments of the external forcing terms (17) and (18), i.e., $\sum_i F_i^{BB/SP}\mathbf{c}_i$. This force can be shown to equate to the total hydrodynamic force on a particle when Eq. (8) is evaluated by substituting the explicit forms of the collision terms.

3.1.1. Chapman-Enskog analysis

The new Eq. (16) is further analysed by means of a Chapman-Enskog analysis to investigate the influence of the external BB and SP forcing terms on the macroscopic conservation equations. For the remainder of the analysis, the Einstein notation is used and a shorter notation is introduced for partial derivatives by expressing $\frac{\partial}{\partial x} = \partial_x$ and $\frac{\partial}{\partial t} = \partial_t$. Furthermore, the distribution function and equilibrium distribution functions are henceforth written as $f_i(\mathbf{x}, t) = f_i$ and $f_i^{eq}(x_\alpha, u_{s,\alpha}, t) = f_i^{eq}(u_{s,\alpha})$, where α indicates one component of a vector, for the sake of readability. After Taylor expansion of $f_i(\mathbf{x} + \mathbf{c}_i\Delta t, t + \Delta t)$ and some algebra, Eq. (16) becomes

$$\Delta t \left(\partial_t + c_{i,\alpha}\partial_\alpha\right) f_i + \mathcal{O}(\Delta t^3) = \Omega_i^{BGK} + F_{i,\alpha} - \frac{\Delta t}{2}\left(\partial_t + c_{i,\alpha}\partial_\alpha\right)\left[\Omega_i^{BGK} + F_{i,\alpha}\right] , \quad (20)$$

where terms of higher order than $\mathcal{O}(\Delta t^3)$ are neglected. The perturbation ansatzes used for the particle distribution function and for the time and space derivatives are

$$f_i = f_i^{(0)} + \epsilon f_i^{(1)} + \epsilon^2 f_i^{(2)} + ... , \quad (21a)$$

$$\partial_t = \epsilon\partial_t^{(1)} + \epsilon^2\partial_t^{(2)} + \epsilon^3\partial_t^{(3)} , \quad (21b)$$

$$\partial_\alpha = \epsilon\partial_\alpha^{(1)} , \quad (21c)$$

respectively. The general ansatz for the forcing term (Halliday et al., 2001) is

$$F_{i,\alpha} = \epsilon F_{i,\alpha}^{(1)} + \epsilon^2 F_{i,\alpha}^{(2)} . \quad (22)$$

Applying the perturbations (21a), (21b), and (21c) on Eq. (20) yields

$$\mathcal{O}\left(\epsilon^0\right) : \; f_i^{(0)} = f_i^{eq}(u_\alpha) . \quad (23)$$

Making use of the relation given by Eq. (23), it is moreover found at higher orders,

$$\mathcal{O}\left(\epsilon^1\right):\ \left(\partial_t^{(1)}+c_{i,\alpha}\partial_\alpha^{(1)}\right)f_i^{(0)}(u_\alpha)=-\frac{1}{\tau}f^{(1)}+\frac{1}{\Delta t}F_{i,\alpha}^{(1)}, \tag{24}$$

$$\mathcal{O}\left(\epsilon^2\right):\ \partial_t^{(2)}f_i^{eq}(u_\alpha)+\left(\partial_t^{(1)}+c_{i,\alpha}\partial_\alpha^{(1)}\right)\left[1-\frac{\Delta t}{2\tau}\right]f_i^{(1)}=-\frac{1}{\tau}f^{(2)}+\frac{1}{\Delta t}F_{i,\alpha}^{(2)} - \frac{1}{2}\left(\partial_t^{(1)}+c_{i,\alpha}\partial_\alpha^{(1)}\right)F_{i,\alpha}^{(1)}\ , \tag{25}$$

and

$$\mathcal{O}\left(\epsilon^3\right):\ \partial_t^{(3)}f^{(1)}+\partial_t^{(2)}f^{(1)}+\left(\partial_t^{(1)}+c_{i,\alpha}\partial_\alpha^{(1)}\right)f_i^{(2)}=-\frac{1}{\tau}f_i^{(3)}+\frac{1}{\Delta t} - \frac{1}{2}\partial_t^{(2)}\left(-\frac{\Delta t}{\tau}f_i^{(1)}+F_{i,\alpha}^{(1)}\right)-\frac{1}{2}\left(\partial_t^{(1)}+c_{i,\alpha}\partial_\alpha^{(1)}\right)\left[-\frac{\Delta t}{\tau}f_i^{(2)}+F_{i,\alpha}^{(2)}\right]\ . \tag{26}$$

To derive the macroscopic conservation equations, the zeroth to first moments of the above perturbed LB equations have to be taken. The zeroth and first moment of Eq. (23) lead to $\sum_i f_i^{(eq)}(u_\alpha)=\rho$ and $\sum_i f_i^{(eq)}(u_\alpha)c_{i,\alpha}=\rho u_\alpha$, respectively. Furthermore, due to $\rho=\sum_i f_i=\sum_i(f_i^{(0)}+\epsilon f_i^{(1)}+\epsilon^2 f_i^{(2)}+...)$ and $\rho u_\alpha=\sum_i f_i c_{i,\alpha}=\sum_i(f_i^{(0)}c_{i,\alpha}+\epsilon f_i^{(1)}c_{i,\alpha}+\epsilon^2 f_i^{(2)}c_{i,\alpha}+...)$, the following restrictions are found:

$$\sum_i f_i^{(n)}=0\ \text{ for }\ n\geq 1\ , \tag{27a}$$

$$\sum_i f_i^{(n)}c_{i,\alpha}=0\ \text{ for }\ n\geq 1\ . \tag{27b}$$

Summation of the zeroth moments of Eqs. (24), (25), and (26) results with

the restrictions of Eq. (27) in:

$$\left(\epsilon\partial_t^{(1)}+\epsilon^2\partial_t^{(2)}+\epsilon^3\partial_t^{(3)}\right)\rho+\epsilon\partial_\alpha^{(1)}\left(\rho u_\alpha\right)$$
$$=\frac{1}{\Delta t}\left[\epsilon\sum_i F_{i,\alpha}^{(1)}+\epsilon^2\sum_i F_{i,\alpha}^{(2)}\right]-\frac{1}{2}\left[\epsilon\partial_t^{(1)}+\epsilon^2\partial_t^{(2)}\right]\epsilon\sum_i F_{i,\alpha}^{(1)}$$
$$-\frac{1}{2}\epsilon^3\partial_t^{(1)}\sum_i F_{i,\alpha}^{(2)}-\frac{1}{2}\epsilon\partial_\alpha^{(1)}\left[\epsilon\sum_i F_{i,\alpha}^{(1)}c_{i,\alpha}+\epsilon^2\sum_i F_{i,\alpha}^{(2)}c_{i,\alpha}\right]. \quad (28)$$

Similarly, the first moments of Eqs. (24), (25), and (26) are summed to give

$$\left(\epsilon\partial_t^{(1)}+\epsilon^2\partial_t^{(2)}+\epsilon^3\partial_t^{(3)}\right)\left[\rho u_\alpha\right]+\epsilon\partial_\beta^{(1)}\Pi_{\alpha\beta}^{(0)}+\left[1-\frac{\Delta t}{2\tau}\right]\epsilon\partial_\beta^{(1)}\epsilon\Pi_{\alpha\beta}^{(1)}$$
$$=-\epsilon\partial_\beta^{(1)}\epsilon^2\Pi_{\alpha\beta}^{(2)}\left[1-\frac{\Delta t}{2\tau}\right]+\frac{1}{\Delta t}\left[\epsilon\sum_i F_{i,\alpha}^{(1)}c_{i,\alpha}+\epsilon^2F_{i,\alpha}^{(2)}c_{i,\alpha}\right]$$
$$-\frac{1}{2}\left[\epsilon\partial_t^{(1)}+\epsilon^2\partial_t^{(2)}\right]\epsilon\sum_i F_{i,\alpha}^{(1)}c_{i,\alpha}-\frac{1}{2}\epsilon\partial_t^{(1)}\epsilon^2\sum F_{i,\alpha}^{(2)}c_{i,\alpha}$$
$$-\frac{1}{2}\epsilon\partial_\beta^{(1)}\left[\epsilon\sum_i F_{i,\alpha}^{(1)}c_{i,\alpha}c_{i,\beta}+\epsilon^2F_{i,\alpha}^{(2)}c_{i,\alpha}c_{i,\beta}\right], \quad (29)$$

where

$$\Pi_{\alpha\beta}^{(0)}=\sum_i f_i^{(0)}c_{i,\alpha}c_{i,\beta}=\rho u_\alpha u_\beta+\rho c_s^2\delta_{\alpha\beta} \quad (30)$$

and $c_s^2=1/3$. The term $\Pi_{\alpha\beta}^{(1)}$ and $\Pi_{\alpha\beta}^{(2)}$ are determined by taking the second moments of Eq. (24) and Eq. (25) (refer to details in the Appendix B) as

$$\Pi_{\alpha\beta}^{(1)}=-\tau\Bigg[c_s^2\rho\left(\partial_\beta^{(1)}u_\alpha+\partial_\alpha^{(1)}u_\beta\right)+\frac{1}{\Delta t}\Bigg(u_\alpha\sum_i F_{i,\beta}^{(1)}c_{i,\beta}+u_\beta\sum_i F_{i,\alpha}^{(1)}c_{i,\alpha}$$
$$-u_\alpha u_\beta\sum_i F_{i,\gamma}^{(1)}+c_s^2\delta_{\alpha\beta}\sum_i F_{i,\gamma}^{(1)}\Bigg)-\frac{1}{\Delta t}\sum_i F_{i,\alpha}^{(1)}c_{i,\alpha}c_{i,\beta}\Bigg], \quad (31)$$

and

$$\epsilon^2\Pi_{\alpha\beta}^{(2)}=\frac{\tau}{\Delta t}\left(\epsilon\sum_i F_{i,\alpha}^{(1)}c_{i,\alpha}c_{i,\beta}+\epsilon^2\sum_i F_{i,\alpha}^{(2)}c_{i,\alpha}c_{i,\beta}\right)+\Re, \quad (32)$$

where $\Re$ contains the terms common between the BB and SP models.

The zeroth to second moments of the perturbed external forcing terms are listed in Table 1, showing identical zeroth and first moments between the BB and SP models. The zeroth moments are zero, meaning that mass

	$F_i^{SP,(1)}$	$F_i^{SP,(2)}$	$F_i^{BB,(1)}$	$F_i^{BB,(2)}$
$\sum_i F_{i,\alpha}^{(n)}$	0	0	0	0
$\sum_i F_{i,\alpha}^{(n)} c_{i,\alpha}$	$B\rho(u_{s,\alpha} - u_\alpha)$	0	$B\rho(u_{s,\alpha} - u_\alpha)$	0
$\sum_i F_{i,\alpha}^{(n)} c_{i,\alpha} c_{i,\beta}$	$B\rho(u_{s,\alpha}u_{s,\beta} - u_\alpha u_\beta)$	0	$B\rho(u_{s,\alpha}u_{s,\beta} - u_\alpha u_\beta)$	$B\frac{\Delta t}{\tau}\Pi_{\alpha\beta}^{(1)}$

Table 1: Zeroth to second moments of perturbed external forcing terms, Eqs. (17) and (18), from the BB and SP models, where $\Pi_{\alpha\beta}^{(1)} = \sum_i f_i^{(1)} c_{i,\alpha} c_{i,\beta}$.

is conserved. The first moments are non-zero, thus affecting the fluid momentum equation. The expressions $B\rho(u_{s,\alpha} - u_\alpha)$ and $B\rho(u_{s,\alpha}u_{s,\beta} - u_\alpha u_\beta)$ can be related to the hydrodynamic force as

$$B\rho(u_{s,\alpha} - u_\alpha) = \frac{\Delta t}{h^d} F_\alpha^{\mathrm{H}} \,, \tag{33}$$

and

$$B\rho(u_{s,\alpha}u_{s,\beta} - u_\alpha u_\beta) = \left(u_\alpha F_\beta^{\mathrm{H}} + u_\beta F_\alpha^{\mathrm{H}} + \frac{\Delta t}{h^d} \frac{F_\alpha^{\mathrm{H}} F_\beta^{\mathrm{H}}}{B\rho} \right) \frac{\Delta t}{h^d} \,. \tag{34}$$

The second moments are different at order $\mathcal{O}(\epsilon^2)$, with the SP result equal to zero while the BB result is non-zero.

Now the macroscopic conservation equations are derived by substituting Eqs. (30) to (32), and the moments listed in Table 1 in combination with Eqs. (33) and (34), into Eqs. (28) and (29). The resulting mass and momentum conservation equations for the SP models are respectively

$$\partial_t \rho + \partial_\alpha \left(\rho u_\alpha \right) = -\frac{1}{2} \frac{\Delta t}{h^d} \partial_\alpha F_\alpha^{\mathrm{H}} \,, \tag{35}$$

and

$$\partial_t(\rho u_\alpha)+\partial_\beta(\rho u_\alpha u_\beta)=-\partial_\alpha p+\partial_\beta\eta_f\left(\partial_\beta u_\alpha+\partial_\alpha u_\beta\right)+\frac{1}{h^d}F_\alpha^{\mathrm{H}} - \frac{\Delta t}{2h^d}\left[\epsilon\partial_t^{(1)}+\epsilon^2\partial_t^{(2)}\right]F_\alpha^{\mathrm{H}}-\left(2\tau-\frac{\Delta t}{2}\right)\partial_\beta\frac{\Delta t}{h^{2d}}\frac{F_\alpha^{\mathrm{H}}F_\beta^{\mathrm{H}}}{B\rho} - \frac{\tau}{h^d}\partial_\beta\left(u_\alpha F_\beta^{\mathrm{H}}+u_\beta F_\alpha^{\mathrm{H}}\right)-\partial_\beta\Re\left(1-\frac{\Delta t}{2\tau}\right)\,, \tag{36}$$

where $p=\rho c_s^2$ and $\eta_f=\left(\tau-\frac{\Delta t}{2}\right)\rho c_s^2$ are the fluid pressure and viscosity respectively. For the BB model, only the momentum equation differs as

$$\partial_t(\rho u_\alpha)+\partial_\beta(\rho u_\alpha u_\beta)=-\partial_\alpha p+\partial_\beta\left[\eta_f+B\tau\rho c_s^2\right]\left(\partial_\beta u_\alpha+\partial_\alpha u_\beta\right)+\frac{1}{h^d}F_\alpha^{\mathrm{H}} - \frac{\Delta t}{2h^d}\left[\epsilon\partial_t^{(1)}+\epsilon^2\partial_t^{(2)}\right]F_\alpha^{\mathrm{H}}-\frac{\Delta t}{2h^d}\partial_\beta^{(1)}\left(u_\alpha F_\beta^{\mathrm{H}}+u_\beta F_\alpha^{\mathrm{H}}\right) - \frac{dt}{h^{2d}}\tau\frac{F_\alpha^{\mathrm{H}}F_\beta^{\mathrm{H}}}{\rho}\left(\frac{1}{B}+1\right) - \frac{\epsilon}{\Delta t}\partial_\beta\sum_i F_{i,\alpha}^{(1)}c_{i,\alpha}c_{i,\beta}-\partial_\beta\Re\left(1-\frac{\Delta t}{\tau}\right)\,. \tag{37}$$

3.1.2. Remarks on the macroscopic conservation equations

Firstly, the forcing term of the SP model, F_i^{SP} of Eq. (18), resembles an external forcing scheme proposed by Kupershtokh et al. (2009),

$$F_i=f_i^{eq}(\rho,\mathbf{u}^{eq}+\Delta\mathbf{u})-f_i^{eq}(\rho,\mathbf{u}^{eq})\,, \tag{38}$$

where it can be shown that $\mathbf{u}^{eq}+\Delta\mathbf{u}=\mathbf{u}_s$ on a solid node. The macroscopic force contribution resulted from the Kupershtokh scheme has been shown (Huang et al., 2011) to be the same as that given by the SP model, i.e., the fifth term of the RHS of Eq. (36). Other terms, such as the derivative of the external force or $u_\alpha F_\beta+u_\beta F_\alpha$ in the mass or momentum equations Eqs. (35) to (37), appear to be due to a missing velocity correction, which may be supplemented using a formulation given by Guo et al. (2002).

Secondly, the error terms due to the external forcing differ between the SP and BB models only when the third $\mathcal{O}(\epsilon^3)$ and higher orders are considered. The most significant discrepancy lies in the stress tensor on the solid covered lattice nodes, which are $\eta_f \left[\partial_\beta u_\alpha + \partial_\alpha u_\beta\right]$ and $\partial_\beta \left[\eta_f + B\tau\rho c_s^2\right] \left(\partial_\beta u_\alpha + \partial_\alpha u_\beta\right)$ for the SP and BB models, respectively. They are both in the form of a Newtonian fluid stress tensor. The one for the BB model is, however, modified in the particle proximity ($B \neq 0$) by an artificially increase of $B\tau\rho c_s^2$ in viscosity. This will affect the fluid velocity computation due to the presence of particles and in turn change the hydrodynamic force calculation for the particles. This effect is tested through simulations of simple shear of particles suspended in a fluid and by validating the stresslet and bulk stress calculation in the subsequent sections.

3.2. Stresslet validation for a single freely moving particle in simple shear flow

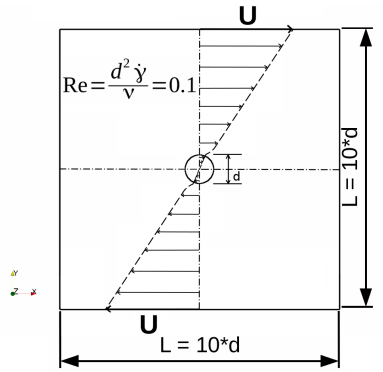

Figure 2: Schematic of the setup of a single particle placed between two shearing walls to validate the stresslet computation. The vectors show the expected stream velocity profile.

In the simplest case, the stresslet computation can be validated by simulating a single particle in a sheared field as illustrated in Fig. 2. The

single sphere stresslet in Stokes flow has an analytical solution (Guazzelli and Morris, 2012)

$$S_{ij} = \frac{20}{3}\pi\eta_f r_p^3 E_{ij} \ , \tag{39}$$

where r_p is the particle radius, η_f the dynamic viscosity of the fluid and E_{ij} is the strain rate tensor. The fluid velocity field around the particle is (Guazzelli and Morris, 2012)

$$u_i = u_i^\infty - \frac{5}{2}r_p^3\frac{x_i(x_j E_{jk} x_k)}{r^5} - \frac{r_p^5}{2}E_{jk}\left[\frac{\delta_{ij}x_k + \delta_{ik}x_j}{r^5} - \frac{5x_i x_j x_k}{r^7}\right] \ , \tag{40}$$

where $r = |\mathbf{x}|$ is the distance from the particle centre and u_i^∞ is the undisturbed fluid velocity. In our simulation, the particle is placed at the coordinate origin in the middle of a domain with the flow in the x_1 direction and the gradient in x_2, resulting in $E_{12} = E_{21} = \frac{1}{2}\dot{\gamma}$ with the shear rate $\dot{\gamma}$. The velocity along the particle centre line is then

$$u_1 = \dot{\gamma}x_2\left(1 - \frac{r_p^5}{2x_2^5}\right) \ . \tag{41}$$

The spin rate in steady state is (Bluemink et al., 2008):

$$\boldsymbol{\Omega}_p = \boldsymbol{\omega}^\infty \ , \tag{42}$$

where $\boldsymbol{\Omega}_p$ is the particle's angular velocity and the fluid rotation vector is $\boldsymbol{\omega}^\infty = \frac{1}{2}\left(\nabla \times \mathbf{u}^\infty\right)$.

Simulations for a range of relaxation time $\tau = [0.6\text{–}1.4]$ with a fixed lattice resolution ($N = 10$ lattice cells over the particle diameter) were performed to test the possible slip velocity due to the BGK collision term (He et al., 1997). The domain of size $\left[\frac{L_1}{d_p} \times \frac{L_2}{d_p} \times \frac{L_3}{d_p}\right] = [10 \times 10 \times 10]$ is periodic in the x (x_1) and z (x_3) directions with solid walls in the y (x_2) direction moving at a fixed velocity imposed through the non-equilibrium

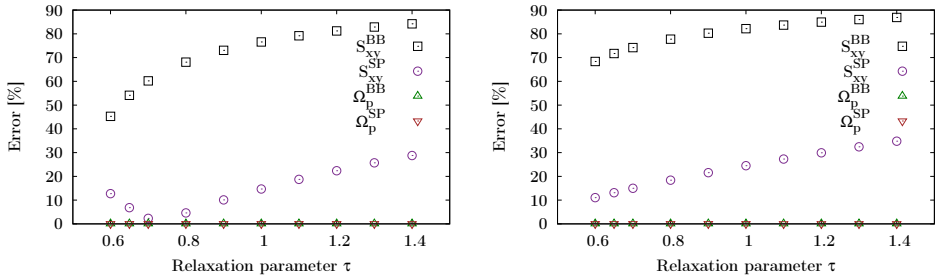

Figure 3: The simulation errors compared to the analytical solutions for the single sphere stresslet S_{xy} and angular velocity errors Ω_p as a function of τ using the (a) linear and (b) non-linear $B(x, \tau)$, for a freely moving particle in a simple shear flow.

bounce back boundary condition (Zou and He, 1997). The particle Reynolds number $Re = 0.1$ and its centre is located exactly at a lattice node.

The difference between the simulation results and the analytical solutions are presented for the BB and SP models using two different weighting functions B (Eqs. (6) and (7)) in Fig. 3. The differences of the angular velocities in steady state are extremely small over the whole relaxation parameter range, demonstrating the accurate solution of the kinematics. However, the stresslet computed using the BB model deviates significantly from the analytical solution, being over 40% for all the parameters tested. The error from the SP model, in contrast, is much lower and can reduce to less than 5% for the relaxation parameters between 0.65 and 0.8. In general, the linear weighting function produces smaller errors, but the erros increase with increasing τ. The results presented in the following use $\tau = 0.7$ and the linear weighting function unless specified otherwise. The stresslet thus proves to be a more stringent test for the LBM's capability to capture suspension rheology. This is not unexpected as the stresslet calculation depends on the

details of the fluid–solid interaction at the interface, the details of which will be examined next.

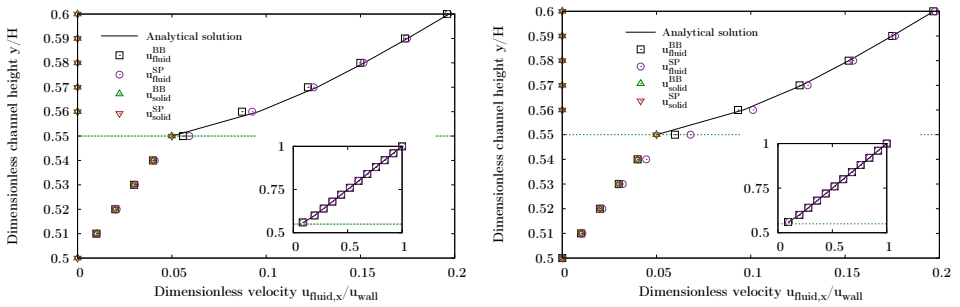

(a) $\tau = 0.7$ (b) $\tau = 1.1$

Figure 4: The x-component of velocities varying along y-axis. The solid line indicates the analytical solution given by Eq. (41). The exact location of the particle surface is indicated by the horizontal (green) dashed line. Inset: Fluid velocity profile for the same simulations shown from particle surface to channel wall, with data plotted on every fourth lattice node.

Solid and fluid velocity profiles (u_x) for two different relaxation parameters, $\tau = 0.7$ and $\tau = 1.1$, are shown in Fig. 4, focusing on the region close to particle surface with the full velocity profiles given in the insets. For both relaxation parameters, the velocity profiles from the simulations show good agreement to the analytical solution for the bulk flow, with growing error closer to the surface. For $\tau = 0.7$, the SP model gives a slightly better agreement to the analytical velocity profile in the close proximity to the surface; the BB model, however, has slightly better agreement with the no-slip condition at and below the particle surface. An increase of the relaxation parameter to $\tau = 1.1$, leads to an increase in the slip velocity on the particle surface, Fig. 4b.

The local hydrodynamic forces on the particle surface, as calculated by

Eq. (8), are examined next. From solving the Stokes equation and using the Newtonian fluid stress constitutive relation, the analytical surface traction can be derived, which can be converted to a hydrodynamic force at every point on the particle surface, $F_{\text{Analytical}}$, by multiplying an appropriate suface area, h^2. This force is used to scale the LBM hydrodynamic force to give a sense of the accuracy of Eq. (8). We note, however, that this comparison is only one aspect of the accuracy of the PSC method because in this method, the fluid–solid momentum transfer is 'smoothed' over a few layers of boundary nodes through the use of the weighting function B. It is therefore useful to present the hydrodynamic force result across the interface as shown in Fig. 5. The local hydrodynamic force at the surface is larger for the SP model, and inside the particle is almost identical to zero for the BB model, Fig. 5. This is consistent with the velocity results in Fig. 4, considering that Eq. (19) indicates that the larger slip velocity, the larger hydrodynamic force. For $\tau = 1.1$ Fig. 5b, the same comparison between the BB and SP models holds; while the force magnitude reduces comparing to that for $\tau = 0.7$, indicating an opposite effect of τ on the hydrodynamic force solution from that on the velocity, Fig. 4b. The force calculated from both models are axial symmetric, resulting in zero total hydrodynamic force on the particle as it should for a freely-moving particle.

In summary, varying the relaxation parameter changes the slip velocities and hydrodynamic forces so that only one narrow relaxation parameter range yields correct results for the SP method, whereas the BB method underestimates the stresslet due to its smaller hydrodynamic forces compared to the SP method.

The stresslet difference between BB and SP has been checked to be not affected by other numerical factors, such as domain size, lattice and subgrid

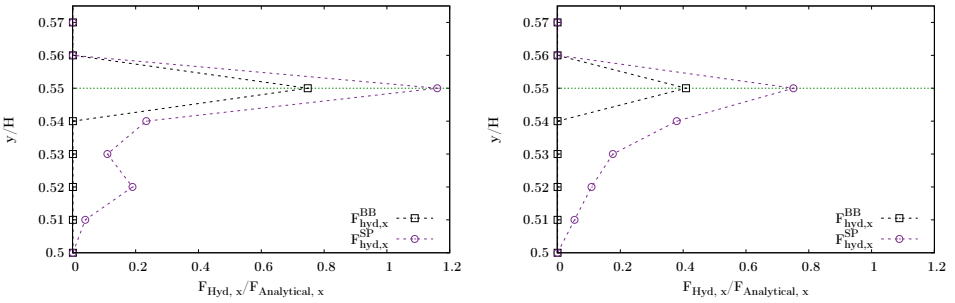

(a) $\tau = 0.7$ (b) $\tau = 1.1$

Figure 5: The x-component of the hydrodynamic force scaled by the value calculated using the analytical surface traction along the y-axis. The exact location of the particle surface is indicated by the horizontal (green) dashed line. Piece-wise linear lines connecting the symbols are used for visual guidance.

resolution. It is indeed caused by the formulation difference and can be understood from the analytical findings in the previous section. As has been shown, the fluid viscosity calculated by the BB model is artificially increased on solid covered lattice nodes, leading to decreased fluid velocities at particle surface and hence smaller hydrodynamic forces and stresslet. The dependence of the artificial viscosity on the relaxation parameter τ, together with using BGK, leads to the dependence of the stresslet error on τ.

The disparity between the errors in the velocity and stresslet calculation is striking, but can nonetheless be understood from the kinetic nature of the lattice Boltzmann method – the kinematics of fluid is resolved, but not coupled to the fluid stress field via a constitutive equation. Physically, one can imagine that an assembly of fluid particles moves at a certain velocity and impinges on a solid surface, being 'reflected' in a certain way according to the boundary conditions. The details of the interaction with the solid boundary may not affect the bulk flow field to a great deal, but can suf-

ficiently alter the local momentum transfer, hence the local hydrodynamic force, leading to different accuracy in fluid velocity and stresslet calculation.

3.3. Torque and stresslet for a fixed particle in simple shear flow

To further verify if the SP model is more accurate than the BB model for stresslet calculation, a fixed particle in simple shear flow was simulated using the same set-up and parameters as in the previous section. This also serves to resolve the seemingly contradicting conclusion in the literature regarding the torque calculation as mentioned in the introduction. For such a case, the hydrodynamic torque on the particle is (Guazzelli and Morris, 2012):

$$T_i = 8\pi\eta_f r_p^3 \omega_i^\infty \ . \tag{43}$$

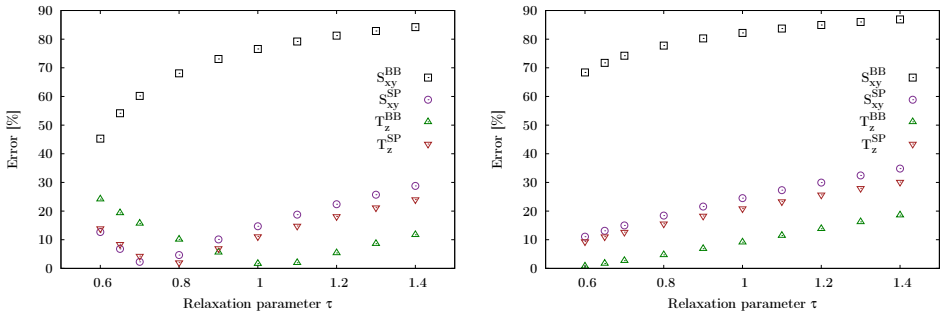

Figure 6: The errors of the single sphere stresslet and torque varying against τ using (a) the linear and (b) non-linear $B(x, \tau)$ for a fixed particle.

The stresslet results compared to the analytical solution are similar to the case of freely moving particle, as shown in Fig. 6, and the conclusion remains the same. The torque results show, however, that the BB model can produce relatively accurate results with a minimum error at $\tau = [0.9 - 1.1]$ using the linear weighting function, comparable to the literature findings.

The SP model consistently produces accurate torque in the same parameter range as for the stresslet calculation. As the torque and the stresslet are respectively the antisymmetric and symmetric parts of the first moment of the hydrodynamic force, $\mathbf{r} \bigotimes \mathbf{F}$, the vastly different accuracies resulted from the BB model seem peculiar.

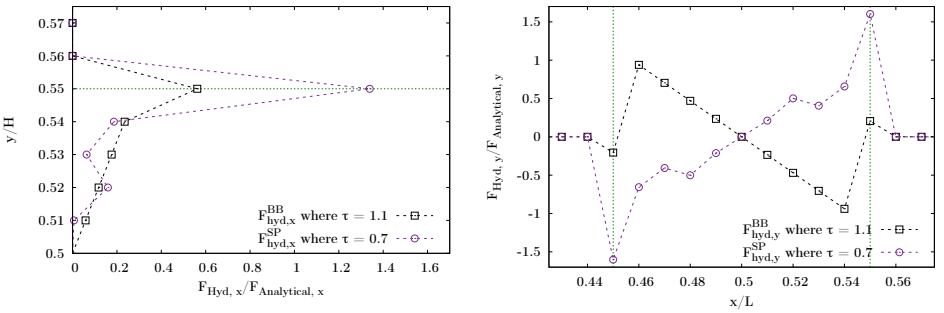

(a) (b)

Figure 7: The hydrodynamic forces scaled by the respective analytical values calculated using the surface traction: (a) the x-component varying along the y-axis and (b)the y-component varying along the x-axis for a fixed particle in simple shear flow. The exact location of the particle surface is indicated by the (green) dashed lines. The relaxation parameter is chosen so that the torque error is minimised. Piece-wise linear lines connecting the symbols are used for visual guidance.

To further understand this, we first examine the hydrodynamic forces, of which the x and y components along the axes are shown in Fig. 7. For both models, the force profiles in x direction along the y axis, Fig. 7a, are comparable to those of the freely rotating sphere (Fig. 5), with slightly larger surface forces. The surface forces in y direction along the x axis, Fig. 7b, are smaller than those in x direction. The force varies monotonically from the surface to the inside of particle for the SP model; but changes direction and increases in magnitude at first for the BB model, which appears to be

unphysical. We then study the components of the dyadic product $\mathbf{F} \bigotimes \mathbf{r}$ in the evaluation of torque (Eq. (9)) $T_z = \sum^{N_{nodes}} (F_y d_x - F_x d_y)$ and stresslet (Eq. (13)) $S_{xy} = \sum^{N_{nodes}} \left(\frac{1}{2} (F_x d_y + F_y d_x) \right)$ and list the numerical results in Table 2. It can be seen that the components (especially $F_x d_y$) calculated

	$0.5F_x d_y(d_y \geq 0)$	$0.5F_x d_y(d_y \leq 0)$	$0.5F_y d_x(d_x \geq 0)$	$0.5F_y d_x(d_x \leq 0)$	S_{xy}	T_z
BB method	0.212	0.212	-0.093	-0.093	0.238	-1.22
SP method	0.423	0.423	0.102	0.102	1.05	-1.284

Table 2: The $\mathbf{r} \bigotimes \mathbf{F}$ components integrated over parts of a fixed sphere in simple shear flow, non-dimensionalised by the analytical stresslet value, where $\frac{T_{\text{analytical}}}{S_{\text{analytical}}} = -1.2$.

from the BB model are substantially smaller in magnitude than those from the SP model, explaining the difference in the stresslet. Due to the sign change in $F_y d_x$, however, the BB model produced a numerically accurate torque value. Combining the above analyses of hydrodynamic forces and moments, it can be concluded that the SP model generates more physically robust results, while the BB model produces less accurate and unphysical forces, which gives rise to accurate torque value by chance numerically.

3.4. Stresslet for two freely rotating particles in simple shear flow

As the first step to generalise to multiple-particles systems, the stresslet calculation for two fixed particles, which interact hydrodynamically in simple shear flow, is investigated. The analytical solution for two particles of radii $r_{p,1}$ and $r_{p,2}$ is (Batchelor and Green, 1972b):

$$S_{ij} = \frac{20}{3} \pi r_{p,1}^3 \eta_f \left(E_{ij}(1 + K^{'}) + E_{kl} \left(\frac{r_i r_k \delta_{jl} + r_j r_k \delta_{il}}{r^2} - \frac{r_k r_l}{r^2} \frac{2}{3} \delta_{ij} \right) L^{'} + E_{kl} \frac{r_k r_l}{r^2} \left(\frac{r_i r_j}{r^2} - \frac{1}{3} \delta_{ij} \right) M^{'} \right), \tag{44}$$

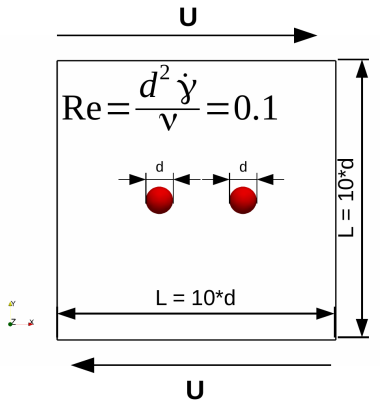

Figure 8: Schematic of the simulation setup of two particles placed between two shearing walls.

where

$$K^{'} = -\frac{r_{p,2}^3(r_{p,1}^2 + r_{p,2}^2)}{r^5} + \mathcal{O}\left(\frac{(r_{p,1} + r_{p,2})^6}{r^6}\right) , \tag{45}$$

$$L^{'} = -\frac{5r_{p,2}^3}{2r^3} + \frac{5r_{p,2}^3(r_{p,1}^2 + r_{p,2}^2)}{r^5} + 25\frac{r_{p,1}^3 r_{p,2}^3}{4r^6} + \mathcal{O}\left(\frac{(r_{p,1} + r_{p,2})^6}{r^6}\right) , \tag{46}$$

$$M^{'} = -\frac{25r_{p,2}^3}{2r^3} + \frac{35r_{p,2}^3(r_{p,1}^2 + r_{p,2}^2)}{r^5} + 25\frac{r_{p,1}^3 r_{p,2}^3}{4r^6} + \mathcal{O}\left(\frac{(r_{p,1} + r_{p,2})^6}{r^6}\right) , \tag{47}$$

and $\mathbf{r}$ is the vector between the particle-particle-centres. The stresslet in simple shear flow using the same coordinate system as before reads

$$S_{xy} = \frac{20}{3}\pi r_{p,1}^3 \eta_f \left(\frac{1}{2}\dot{\gamma}(1 + K^{'}) + \frac{1}{2}\dot{\gamma}\frac{r_x r_x + r_y r_y}{r^2}L^{'} + \dot{\gamma}\left(\frac{r_x r_y}{r^2}\right)^2 M^{'}\right) . \tag{48}$$

The simulation setup and numerical parameters are the same as in the single particle case, except the positions of particles, as illustrated in Fig. 8.

The difference between the simulation results and the analytical solution is shown in Fig. 9. The BB model cannot capture the stresslet accurately, showing a minimum discrepancy of more than 40% at $\tau = 0.6$ and using the linear weighting function. In contrast, the SP model produce an error less

than 5% around $\tau = 0.65 - 0.8$ using the linear weighting function. Using the non-linear weighting function results in increased errors, similarly to the single sphere case.

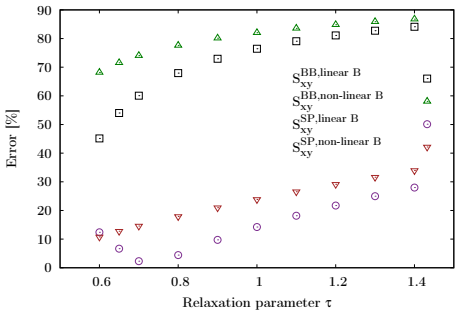

Figure 9: The errors of the simulated stresslet compared to the analytical solution for a pair of freely rotating particles in shear flow against the relaxation parameter τ for models BB and SP with different weighting functions B.

3.5. Stresslet contribution to bulk viscosity of sheared suspensions

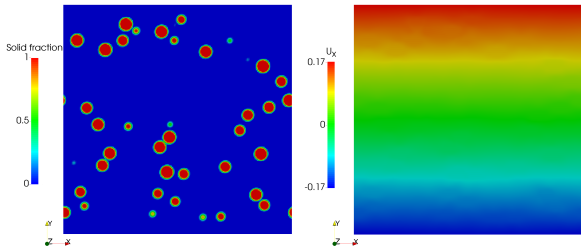

Figure 10: 3D simulation of a sheared suspension of solid fraction $\phi = 0.05$ is illustrated on a slice through the domain. The distribution of particles indicated by the solid fractions is shown on the left and the fluid velocity component in horizontal direction on the right.

Hitherto, the numerical errors of using the BB and SP models have been quantified at the particle scale. In this section, we demonstrate the effect

on the computation of suspension bulk viscosity. To this end, simulations of homogeneous simple shear of many particles were performed with an imposed shear rate at the low Reynolds number regime, i.e. $Re = \frac{d_p^2 \dot{\gamma}}{\nu} < 1$. The simple shear was realised by imposing the Lees-Edwards boundary condition (Lees and Edwards, 1972) to both the DEM and LBM (Wagner and Pagonabarraga, 2002) on a three dimensional periodic simulation domain. We simulate around 500 neutrally buoyant frictionless mono-disperse particles suspended in a Newtonian fluid. Typical results of solid volume fraction and fluid velocity distributions are illustrated on a cross section in Fig. 10. Different solid fractions were obtained by varying the domain size in the range $\left[\frac{L_1}{d_p} \times \frac{L_2}{d_p} \times \frac{L_3}{d_p}\right] \geq [10 \times 10 \times 10]$. The maximum solid fraction was capped at $\phi_{\max} = 0.25$ to focus on the stresslet contribution and minimise particle–particle mechanical contact and lubrication interaction, which is unresolved below the lattice resolution. When particles come into solid contact, a Hookean spring contact model was employed and the resulting stress was computed (Thompson et al., 2009). The spring stiffness was chosen to be high enough to keep the rheology in the hard-sphere regime, i.e., the stiffness does not affect the obtained rheology. The lattice resolution was set to $N = 10$ lattice nodes over a particle diameter and the relaxation parameter $\tau = 0.65$ was chosen. The particle stresslet contribution to the bulk stress can be calculated by summing up the stresslet due to both the hydrodynamic and contact interactions.

The viscosity of hard-sphere suspensions in the quasi-Newtonian regime is known to increase with the solid volume fraction ϕ and scale with the fluid viscosity η_f. We thus focus on studying the relative suspension viscosity, $\eta_r = \eta/\eta_f$, as a function of ϕ. At the infinitely dilute limit with non-interacting hard spheres, Einstein showed that the single particle stresslet

increases the suspension viscosity as a linear function of the volume fraction, $\eta_r = 1 + 2.5\phi$, which is a good approximation for $\phi < 0.01$. At higher concentration the hydrodynamic interactions between particles become important, Batchelor and Green (1972a) calculated the effect of two-sphere hydrodynamic interaction and obtained

$$\eta_r = 1 + 2.5\phi + 7.6\phi^2 \ , \tag{49}$$

which is valid for $\phi < 0.1$. For even higher concentrations, multibody interactions become imperative and a first-principle model is still lacking. Phenomenological equations have been introduced to correlate the viscosity of concentrated suspensions to the solid volume fraction. Krieger and Dougherty (1959) proposed a semi-empirical correlation

$$\eta_r = \left(1 - \frac{\phi}{\phi_{\max}}\right)^{-[\eta]\phi_{\max}} \ , \tag{50}$$

where the intrinsic viscosity $[\eta]$ and maximum packing fraction $\phi_{\max}$ have to be determined by comparison to experiments in general. For mono-disperse spheres $[\eta] = 2.5$ according to Einstein's equation. We use the experimental data from (van der Werff and de Kruif, 1989) to indicate the experimental trend for nearly mono-disperse hard-sphere suspensions with $\phi_{\max,\mathrm{mono}} = 0.63$ and $[\eta]\phi_{\max,\mathrm{mono}} = 2$ while keeping in mind the sensitivity to particle size distribution and surface interactions, which are unavoidable in experiments.

We first confirm that the hydrodynamic stresslet contribution to the suspension viscosity indeed dominates over that from particle contacts in the range of volume fraction probed for both the BB and SP models, although the contact contribution grows from about 1% to 20% of the total contribution as the volume fraction increases due to a growing probability

of particle contacts. The accuracy of the stresslet computation, as discussed in the previous sections, is therefore expected to largely affect the bulk viscosity. Indeed the results from the BB model are significantly smaller than

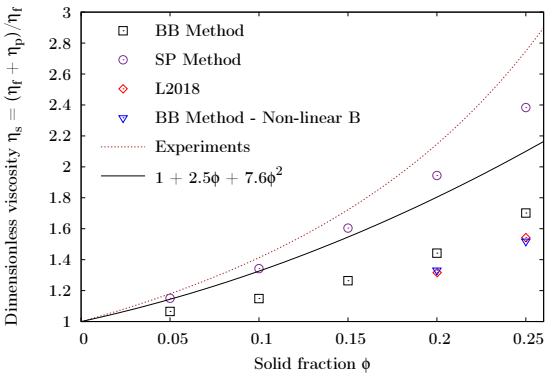

Figure 11: Relative suspension viscosity varying against the solid fractions of sheared suspensions of frictionless mono-disperse particles. Extracted data from Lorenz et al. (2018), abbreviated as L2018 in the legend, is included for comparison.

the SP model results at all volume fractions, although both predict the increasing trend with respect to volume fraction, as shown in Fig. 11. The SP viscosity at $\phi \leq 0.1$ is in excellent agreement with the appropriate analytical result of Batchelor and Green (1972a), Eq. (49). For $\phi > 0.1$, the SP method predicts viscosities in good agreement with experimental results, and higher than those of Eq. (49) as it should, because the LBM simulation takes into account multibody hydrodynamic interactions (HI), while Eq. (49) only captures the two-particle HI. In contrast, the BB method significantly under-predicts the viscosity at all volume fractions. The magnitudes of the discrepancy at lower volume fractions, about 40% of the correct values, are comparable to those shown for the single and pair particle stresslets as expected. At higher volume fractions, the error grows larger and the values are less than the predictions of Eq. (49), indicating that the same type of errors

also affect the multibody HI. In this sense the contrast between the SP and BB models at $\phi > 0.1$ is more physically significant, the former correctly reveals the effect of multibody HI, while the latter completely disguises the effect.

In addition, results from independent simulations (Lorenz et al., 2018) employing the same methodology using the BB model with the non-linear solid fraction weighting function Eq. (7) are compared. The results, indicated by the diamonds in Fig. 11, are in close agreement with our results, further confirming our findings on the BB model. Furthemore, it shall be remarked that the viscosity predicted by the SP method is still somewhat lower than the experimental results at $\phi > 0.1$. This can be attributed to the unresolved lubrication forces, which become more important as more particles can come into close separations at higher volume fractions. The further lubrication force contribution would be expected to increase the suspension viscosity and lead to better agreement between simulation and the experimental results (van der Werff and de Kruif, 1989). The lubrication force correction in this PSC LBM coupling methodology will be discussed in a future publication.

4. Conclusions

The partially-saturated-cell (PSC) method for lattice-Boltzmann simulation of particle–fluid flows has been analysed theoretically and numerically, comparing the non-equilibrium bounce back (BB) and the superposition (SP) models in their capability of accurately computing the hydrodynamic stresslet. The theoretical analysis has demonstrated that the PSC method can be recast into a single phase LB equation supplemented with an external

forcing term, which is equivalent to the Kuperstokh forcing only in case of the SP model. The macroscopic momentum conservation equation obtained from the BB model contains an artificial viscosity on solid covered lattice nodes, depending on the solid fraction, the relaxation parameter, density, and speed of sound.

Numerical simulations have shown that the SP model can predict the stresslet within 5% of error using the relaxation parameter τ between 0.65 and 0.8; whereas the BB model results in discrepancies of at least 40% compared to the analytical solution at the single and the pair particle levels. The different performance lies essentially in their hydrodynamic force computation, where the SP model yields physically sound forces with larger magnitudes at the particle–fluid interface. The inaccuracy of the BB model leads to significant underestimation of the bulk viscosity in dilute suspensions as compared to analytical and experimental results. It is therefore recommended that the SP method is employed in the PSC LBM simulations of suspensions.

This work also highlights the need to further improve the solid collision models and the formulation of the local hydrodynamic force (Eq. (8)); so that the errors in the hydrodynamic force, hence the stresslet calculation can be reduced for all relaxation parameters. This warrants substantial future work in this direction.

Acknowledgement

We thank Timm Krüger and Oliver Henrich for very helpful discussions and pointing out the resemblance between the investigated methodology and a Kuperstokh forcing scheme. TN would like to acknowledge a Marie

Skłodowska-Curie early career fellowship funded by the European Union's Seventh Framework Programme under grant agreement no. ITN607453. JS would like to acknowledge support from the UK Engineering and Physical Sciences Research Council (EPSRC) EP/N025318/1, the UK Natural Environment Research Council (NERC) NE/R011001/1, The Royal Academy of Engineering/The Leverhulme Trust Senior Research Fellowship LTSRF1617/13/2 and The National Natural Science Foundation of China grant 4728006. All data used within this publication can be accessed at: https://doi.org/10.7488/ds/2553.

Appendix A. Modified non-equilibrium bounce back solid phase collision term for PSM

The modification by Holdych (2003) to the non-equilibrium bounce back solid phase collision term Eq. (4) (Noble and Torcyznski, 1998) was achieved by substituting the fluid velocity by the particle velocity in the equation, resulting

$$\Omega_i^s = f_{-i} - f_i + f_i^{eq}(\mathbf{u}_s) - f_{-i}^{eq}(\mathbf{u}_s) \; . \tag{A.1}$$

However, numerical instability issues have been reported in the literature as well as in our work. A possible mechanism leading to the instability is analysed here. Substituting the solid phase collision term Eq. (A.1) into the hydrodynamic force Eq. (8) leads to, on a $D2Q9$ lattice,

$$F_{hyd,\alpha}^{Holdych} = \frac{h^d}{\Delta t} \sum_n B_n \cdot 2 \cdot \rho(u_{s,\alpha} - u_\alpha) \; . \tag{A.2}$$

Eq. (A.2) gives exactly twice as much hydrodynamic force as that by Eq. (19) according to the Noble and Torcyznski (1998) model. It was found that the modified non-equilibrium bounce back method Eq. (A.1) can simulate fixed particles, but leads to instability for freely moving particles due to

the doubled hydrodynamic forces and torques on the particles. In fact, if Eq. (A.1) is multiplied by a factor of 0.5, the normal hydrodynamic force and stability in simulations of freely moving particles are recovered.

Appendix B. Evaluation of $\Pi^{(1)}_{\alpha\beta}$

$$\Pi^{(1)}_{\alpha\beta} = \tau \left[-\partial^{(1)}_t \Pi^{(0)}_{\alpha\beta} - \partial^{(1)}_\gamma \Pi^{(0)}_{\alpha\beta\gamma} + \frac{1}{\Delta t} \sum_i F^{(1)}_{i,\alpha} c_{i,\alpha} c_{i,\beta} \right] . \tag{B.1}$$

The derivation of the time differential $\partial^{(1)}_t \Pi^{(0)}_{\alpha\beta}$ and space differential $\partial^{(1)}_\gamma \Pi^{(0)}_{\alpha\beta\gamma}$ without applied external forces has been detailed in the literature, e.g., by Krüger et al. (2017). Analogously, the derivation of the derivatives with an imposed external forcing term is performed here. The third moment of the equilibrium function is $\Pi^{(0)}_{\alpha\beta\gamma} = f^{(eq)}_i c_{i,\alpha} c_{i,\beta} c_{i,\gamma} = \rho c_s^2 (u_\alpha \delta_{\beta\gamma} + u_\beta \delta_{\alpha\gamma} + u_\gamma \delta_{\alpha\beta})$ and the derivative can be written as

$$\partial^{(1)}_\gamma \Pi^{(0)}_{\alpha\beta\gamma} = c_s^2 \left(\partial^{(1)}_\beta (\rho u_\alpha) + \partial^{(1)}_\alpha (\rho u_\beta) \right) + c_s^2 \delta_{\alpha\beta} \partial^{(1)}_\gamma (\rho u_\gamma) . \tag{B.2}$$

The expression $\partial^{(1)}_t \Pi^{(0)}_{\alpha\beta}$ can be evaluated by making use of the product rule, $\partial_*(abc) = a\partial_*(bc) + b\partial_*(ac) - ab\partial_* c$ and by rearranging the zeroth and first moments of Eq. (24)

$$\partial^{(1)}_t \rho = -\partial^{(1)}_\alpha (\rho u_\alpha) + \frac{1}{\Delta t} \sum_i F^{(1)}_{i,\alpha} , \tag{B.3a}$$

$$\partial^{(1)}_t (\rho u_\alpha) = -\partial^{(1)}_\beta \Pi^{(0)}_{\alpha\beta} + \frac{1}{\Delta t} \sum_i F^{(1)}_{i,\alpha} c_{i,\alpha} . \tag{B.3b}$$

It follows for $\partial_t^{(1)}\Pi_{\alpha\beta}^{(0)}$ from Eq. (30)

$$\begin{aligned}\partial_t^{(1)}\Pi_{\alpha\beta}^{(0)} &= \partial_t^{(1)}\left(\rho u_\alpha u_\beta + \rho c_s^2\delta_{\alpha\beta}\right)\\ &= -\partial_\gamma^{(1)}(u_\alpha u_\beta u_\gamma) + \frac{1}{\Delta t}\Bigg[u_\alpha\sum_i F_{i,\beta}^{(1)}c_{i,\beta} + u_\beta\sum_i F_{i,\alpha}^{(1)}c_{i,\alpha}\\ &\quad -u_\alpha u_\beta\sum F_{i,\gamma}^{(1)} + c_s^2\delta_{\alpha\beta}\sum_i F_{i,\gamma}^{(1)}\Bigg]\\ &\quad - c_s^2\left[u_\alpha\partial_\beta^{(1)}\rho + u_\beta\partial_\alpha^{(1)}\rho\right] - c_s^2\delta_{\alpha\beta}\partial_\gamma^{(1)}(\rho u_\gamma)\end{aligned} \tag{B.4}$$

Substitution of Eq. (B.4) and Eq. (B.2) with $c_s^2(\partial_\beta^{(1)}(\rho u_\alpha) + \partial_\alpha^{(1)}(\rho u_\beta)) = c_s^2\rho(\partial_\beta^{(1)}u_\alpha + \partial_\alpha^{(1)}u_\beta) + c_s^2(u_\alpha\partial_\beta^{(1)}\rho + u_\beta\partial_\alpha^{(1)}\rho)$ into Eq. (B.1) gives finally

$$\begin{aligned}\Pi_{\alpha\beta}^{(1)} = -\tau\Bigg[&c_s^2\rho\left(\partial_\beta^{(1)}u_\alpha + \partial_\alpha^{(1)}u_\beta\right) - \partial_\gamma^{(1)}\left(u_\alpha u_\beta u_\gamma\right)\\ &+\frac{1}{\Delta t}\Bigg(u_\alpha\sum_i F_{i,\beta}^{(1)}c_{i,\beta} + u_\beta\sum_i F_{i,\alpha}^{(1)}c_{i,\alpha}\\ &-u_\alpha u_\beta\sum_i F_{i,\gamma}^{(1)} + c_s^2\delta_{\alpha\beta}\sum_i F_{i,\gamma}^{(1)}\Bigg)\\ &-\frac{1}{\Delta t}\sum_i F_{i,\alpha}^{(1)}c_{i,\alpha}c_{i,\beta}\Bigg]\end{aligned} \tag{B.5}$$

The term $\partial_\gamma^{(1)}\left(u_\alpha u_\beta u_\gamma\right)$ in the remainder of this analysis is neglected as it is assumed that $u^2 << c_s^2$, i.e., the Mach number is $Ma = \frac{u}{c_s} << 1$.

References

Aidun, C.K., Lu, Y., 1995. Lattice Boltzmann simulation of solid particles suspended in fluid. Journal of Statistical Physics 81, 49–61.

Aidun, C.K., Lu, Y., Ding, E.J., 1998. Direct analysis of particulate suspensions with inertia using the discrete Boltzmann equation. Journal of Fluid Mechanics 373, 287–311.

Batchelor, G.K., 1970. The stress system in a suspension of force-free particles. Journal of Fluid Mechanics 41, 545–570.

Batchelor, G.K., Green, J.T., 1972a. The determination of the bulk stress in a suspension of spherical particles to order c^2. Journal of Fluid Mechanics 56, 401–427.

Batchelor, G.K., Green, J.T., 1972b. The hydrodynamic interaction of two small freely-moving spheres in a linear flow field. Journal of Fluid Mechanics 56, 375–400.

Bhatnagar, P., Gross, E.P., Krook, M., 1954. A model for collision processes in gases. I. Small amplitude processes in charged and neutral one-component systems. Physical Review 94, 511–525.

Bluemink, J.J., Lohse, D., Prosperetti, A., Van Wijngaarden, L., 2008. A sphere in a uniformly rotating or shearing flow. Journal of Fluid Mechanics 600, 201–233.

Chen, S., Doolen, G.D., 1998. Lattice Boltzmann method for fluid flows. Annual Review of Fluid Mechanics 30, 329–364.

Cook, B.K., Bout, D.F., Strack, O.E., Williams, J.R., Johnson, S.M., 2004. DEM-fluid model development for near-wellbore mechanics, in: Shimizu, Y., Hart, R., Cundall, P. (Eds.), Numerical Modeling Micromechanics via Particle Methods - 2004 Proceedings of the 2nd International PFC Symposium, Kyoto, Japan. CRC Press. chapter 37, pp. 301–309.

Cundall, P.A., Strack, O.D.L., 1979. A discrete numerical model for granular assemblies. Geotechnique 29, 47–65.

Daghoogi, M., Borazjani, I., 2015. The influence of inertia on the rheology of a periodic suspension of neutrally buoyant rigid ellipsoids. Journal of Fluid Mechanics 781, 506–549.

Feng, Z.G., Michaelides, E.E., 2005. Proteus: A direct forcing method in the simulations of particulate flows. Journal of Computational Physics 202, 20–51.

Guazzelli, É., Morris, J., 2012. A physical introduction to suspension dynamics. Cambridge Texts in Applied Mathematics (Book 45), Cambridge University Press.

Guo, Z., Zheng, C., Shi, B., 2002. Discrete lattice effects on the forcing term in the lattice Boltzmann method. Physical Review E 65, 046308.

Haddadi, H., Morris, J.F., 2014. Microstructure and rheology of finite inertia neutrally buoyant suspensions. Journal of Fluid Mechanics 749, 431–459.

Halliday, I., Hammond, L.A., Care, C.M., Good, K., Stevens, A., 2001. Lattice Boltzmann equation hydrodynamics. Physical Review E 64, 011208.

He, X., Zou, Q., Luo, l.S., Dembo, M., 1997. Analytic solutions of simple flows and analysis of nonslip boundary conditions for the lattice Boltzmann BGK model. Journal of Statistical Physics 87, 115–136.

Holdych, D.J., 2003. Lattice Boltzmann methods for diffuse and mobile interfaces. Ph.D. thesis. Graduate College of the University of Illinois.

Huang, H., Krafczyk, M., Lu, X., 2011. Forcing term in single-phase and Shan-Chen-type multiphase Boltzmann models. Physical Review E 84, 046710.

Krieger, I.M., Dougherty, T.J., 1959. A mechanism for non-Newtonian flow in suspensions of rigid spheres. Transactions of the Society of Rheology 3, 137–152.

Krüger, T., Kusumaatmaja, H., Kuzmin, A., Shardt, O., Silva, G., Viggen, E.M., 2017. The Lattice Boltzmann Method - Principles and Practice. Springer International Publishing.

Kupershtokh, A.L., Medvedev, D.A., Karpov, D.I., 2009. On equations of state in a lattice Boltzmann method. Computers and Mathematics with Applications 58, 965–974.

Ladd, A.J.C., 1994a. Numerical simulation of particulate suspensions via a discretized Boltzmann equation. Part 1. Theoretical foundation. Journal of Fluid Mechanics 271, 285–309.

Ladd, A.J.C., 1994b. Numerical simulations of particulate suspensions via a discretized Boltzmann equation. Part 2. Numerical results. Journal of Fluid Mechanics 271, 311–339.

Lees, A.W., Edwards, S.F., 1972. The computer study of transport processes under extreme conditions. Journal of Physics C: Solid State Physics 5, 1921–1929.

Lorenz, E., Sivadasan, V., Bonn, D., Hoekstra, A.G., 2018. Combined lattice-Boltzmann and rigid-body method for simulations of shear-thickening dense suspensions of hard particles. Computers and Fluids 172, 474–482.

Noble, D.R., Torcyznski, J.R., 1998. A lattice-Boltzmann method for par-

tially saturated computational cells. International Journal of Modern Physics 9, 1189–1201.

Owen, D.R.J., Leonardi, C.R., Feng, Y.T., 2011. An efficient framework for fluid-structure interaction using lattice Boltzmann method and immersed moving boundaries. International Journal for Numerical Methods in Engineering 87, 66–95.

Seil, P., 2016. LBDEMcoupling: Implementation, Validation, and Applications of a Coupled Open-Source Solver for Fluid-Particle Systems. Ph.D. thesis. Department for Particulate Flow Modelling, Johannes Kepler Universität Linz.

Succi, S., 2001. The Lattice Boltzmann Equation: For Fluid Dynamics and Beyond. Numerical Mathematics and Scientific Computation, Clarendon Press.

Thompson, A.P., Plimpton, S.J., Mattson, W., 2009. General formulation of pressure and stress tensor for arbitrary many-body interaction potentials under periodic boundary conditions. The Journal of Chemical Physics 131, 154107.

Wagner, A.J., Pagonabarraga, I., 2002. Lees-Edwards boundary conditions for lattice Boltzmann. Journal of Statistical Physics 107, 521–537.

Wang, M., Feng, Y.T., Wang, C.Y., 2016. Coupled bonded particle and lattice Boltzmann method for modelling fluid-solid interaction. International Journal for Numerical and Analytical Methods in Geomechanics 40, 1383–1401.

van der Werff, J.C., de Kruif, C.G., 1989. Hard-sphere colloidal dispersion: The scaling of rheological properties with particle size, volume fraction, and shear rate. Journal of Rheology 33, 421–454.

Zhou, G., Wang, L., Wang, X., Ge, W., 2011. Galilean-invariant algorithm coupling immersed moving boundary conditions and Lees-Edwards boundary conditions. Physical Review E 84, 066701.

Zou, Q., He, X., 1997. On pressure and velocity boundary conditions for the lattice Boltzmann BGK model. Physics of Fluids 9, 1591–1598.